Journal of Materials Chemistry A

ROYAL SOCIETY OF CHEMISTRY

PAPER

View Article Online
View Journal

Cite this: DOI: 10.1039/d1ta02616j

First-principles formulation of spinel-like structured $Li_{(4-3x)}Y_xCl_4$ as promising solid-state electrolytes to enable superb lithium ion conductivity and matching oxidation potentials to high-voltage cathodes†

Yuanyuan Huang, [abc] Yuran Yu, [abc] Hongjie Xu, [abc] Xiangdan Zhang, [abc] Zhuo Wang*[abc] and Guosheng Shao *[abc]

Received 30th March 2021
Accepted 3rd June 2021

DOI: 10.1039/d1ta02616j

rsc.li/materials-a

Halide solid-state electrolytes (SSEs) have attracted great attention as potential electrolytes for all solid-state batteries (ASSBs) owing to their high oxidation potentials, excellent ductility, and good resilience to humidity. However, to date most reported halide SSEs only demonstrated rather limited ionic conductivities due to lack of effective diffusion channels for fast transportation of lithium ions. Here in this work, we have carried out extensive first principles calculations towards identifying novel candidates as highly attractive halide SSEs, and we find that through tuning the lattice chemistry in the hexagonal Li_3YCl_6 halide, one is able to open a new avenue in achieving three highly stable compounds with spinel-like cubic structures. The two best cubic compounds, $Li_{2.125}Y_{0.625}Cl_4$ and $Li_{2.5}Y_{0.5}Cl_4$, are able to offer very efficient three-dimensional highways for Li^+ transportation, with their being able to offer remarkable room-temperature Li^+ conductivities of 6.11 mS cm^{-1} and 8.42 mS cm^{-1} at low activation energies (0.247 eV and 0.244 eV), respectively. In addition to ionic conductivities being several times higher than that of the pristine Li_3YCl_6 phase, they also have remarkably high oxidation potentials above 4.0 V desirable to accommodate high voltage cathode materials electrochemically.

Introduction

Great efforts have been made in developing solid-state electrolytes (SSEs) with ionic conductivity rivaling that of the current liquid electrolytes, so that all solid-state lithium ion batteries (ASSBs) can be enabled as safe batteries with higher energy densities.[1,2] To date, the main efforts have been in developing SSEs for lithium ion batteries (LIBs), particularly in developing electrolytes based on oxides and sulfides.[3–6]

The oxide SSEs have distinguished advantages including wide electrochemical windows,[7] good chemical stability,[8] and low sensitivity to air or moisture,[9] though they are notorious for low ionic conductivity (below 0.1 mS cm^{-1} at room temperature),[10] and serious grain/particle boundary issues.[11] Their high synthesis temperature (over 1000 °C),[12] serious brittleness and poor deformability impose further difficulty for manufacturing.[13]

On the other hand, sulfide SSEs have many promising merits including excellent Li^+ ion conductivity,[14] less serious grain boundary issues, low processing temperature (around 500 °C),[15] and easy processes for full-cell fabrication owing to good mechanical deformability.[16] Their main shortcomings are high sensitivity to humid air,[17] and very narrow electrochemical windows incompatible with most practical cathode materials and the lithium anode.[18]

Halide salts are another family of SSEs whose use can be traced back to the 1970s,[19–21] but they were then recognized as very poor ionic conductors with various issues such as huge grain or particle boundary resistance and poor phase stability. The development of halide SSEs was very slow until a significant step forward with the discovery of Li_3MX_6 class of materials (M^{3+}: trivalent metal ions; X: Cl/Br). The room temperature (RT) Li^+ conductivities in Li_3YCl_6 (space group of $P\bar{3}m1$) and Li_3YBr_6 (space group of $C2/m$) reached 0.51 mS cm^{-1} (with activation energy E_a = 0.37 eV) and 1.7 mS cm^{-1} (with E_a = 0.40 eV).[22] Subsequently, substitution of Y by In led to the successful synthesis of Li_3InCl_6 *via* an aqueous route, which showed a much better RT Li^+ conductivity of 2.04 mS cm^{-1} and an activation barrier around 0.35 eV.[23]

[a]School of Material Science and Engineering, Zhengzhou University, Zhengzhou 450001, China. E-mail: wangzh@zzu.edu.cn; gsshao@zzu.edu.cn

[b]State Center for International Cooperation on Designer Low-Carbon & Environmental Materials (CDLCEM), Zhengzhou University, 100 Kexue Avenue, Zhengzhou 450001, China

[c]Zhengzhou Materials Genome Institute, Building 2, Zhongyuanzhigu, Xingyang 450100, China

† Electronic supplementary information (ESI) available. See DOI: 10.1039/d1ta02616j

From the materials design point of view, the major advantages of halide-based SSEs include: (a) the ionic radii of halogen anions (r_{-Cl^-} = 167 pm, r_{-Br^-} = 182 pm, r_{-I^-} = 206 pm) are considerably larger than those of chalcogen ones ($r_{-O^{2-}}$ = 126 pm, $r_{-S^{2-}}$ = 170 pm),[24] which is beneficial in terms of weaker electrostatic attraction to Li^+, and the longer ionic bonds are useful for lattice softening and better ductility;[6,25] (b) the higher oxidation potential of lithium halides than that of sulfides is useful to put up with high-voltage cathodes;[26] (c) most inorganic metal halides are stable in dry air even at elevated temperatures,[22] and (d) low sensitivity to humidity.[27]

To date, efforts have been focused on varying the occupancy of the M^{+3} lattice sites in Li_3MX_6 (Li3/1/6), such as mixing of In and Y,[28] or full occupancy of M^{3+} sites by In,[22,27,29,30] which resulted in stabilized cubic structures (space group $P\bar{3}m1$). The cubic phase was found to be quite tolerant to humidity, while permitting advantageous three-dimensional (3D) transportation of Li^+. One notes, however, that the best RT conductivity, about 2 mS cm^{-1}, together with quite significant activation energy over 0.35 eV for Li^+ transportation is still short of the requirement for practical batteries, since an activation energy this high implies great difficulty for ionic transportation even around the zero Celsius temperatures.

It is noted that in the vicinity of the above Li3/1/6 SSE system, a family of Li_2MCl_4 (M: Cr, Mg, V, Mn, Fe, Cd) (Li2/1/4) halides were discovered in 1986,[31] with every member being of the cubic spinel-type structures.[32] These materials showed attractive ionic conductivity at moderately elevated temperature above 330 °C. For example, the spinel Li_2CrCl_4 with a symmetry of $Fd\bar{3}m(227)$ demonstrated a high ionic conductivity of 63 mS cm^{-1} at 400 °C, and according to its reasonably small activation energy of 0.249 eV, the 300 K ionic conductivity can be derived by extrapolation as about 1 mS cm^{-1}.[32] Recently, a cubic spinel-like $Li_2Sc_{2/3}Cl_4$ was synthesized by a simple co-melting strategy from LiCl and $ScCl_3$.[33,34] In the structure of $Li_2Sc_{2/3}Cl_4$, Li^+ ions occupy about a third of the Sc^{3+} sites, which exhibited an ionic conductivity of 1.5 mS cm^{-1} at room temperature and a moderate activation energy around 0.34 eV. Overall, one can see that the above two families of halide SSEs could achieve similar ionic conductivities at room temperature about 1–2 mS cm^{-1}, and among them those of better RT ionic conductivities showed higher activation barriers. It is therefore desirable for one to devise SSEs of both high RT ionic conductivities and low activation energies at the same time, so that practical batteries could function effectively well below the freezing temperatures.[5,35,36]

Here in this work, we focus on identifying potential ways for further improvement in terms of significant enhancement of ionic conductivities at and below the room temperature. We find that remarkable enhancement of the RT ionic conductivities can be achieved at fairly low activation energies. We have identified stable spinel-like structures based on $Li_{2.125}Y_{0.625}Cl_4$ and $Li_{2.5}Y_{0.5}Cl_4$, which have RT ionic conductivities of 6.11 and 8.42 mS cm^{-1}, respectively. Their low activation energies below 0.247 eV ensure acceptable ionic conductivities above 1 mS cm^{-1} even at −20 °C.

Method

An extensive review of methods for first-principles formulation of battery materials in the framework of the density functional theory (DFT) has been carried out recently.[37] For DFT calculations, we used the Vienna *Ab Initio* Simulation Package (VASP),[5,38–40] with the projector augmented wave (PAW) method for ionic potentials including the effect of core electrons.[41–43] Structure–energy calculations were carried out using the Perdew–Burke–Ernzerhof (PBE) functionals for exchange-correlation (XC).[36,44,45] For geometric relaxation of the structures, summation over the Brillouin zone (BZ) was performed with the Monkhorst–Pack *k*-point intervals limited below 0.04 $Å^{-1}$.[46–48] A plane-wave energy cutoff of 600 eV was used in all calculations.[49,50] For the calculations of energy band structures, we used the HSE06 functional for improved accuracy for bandgaps with consideration of non-local contribution to XC.[51] We employed a convergence criterion of 10^{-6} eV, suitable for electronic self-consistent cycles,[52] with spin polarization being taken into account for all simulations.

Phase diagrams are constructed to assess phase equilibria with respect to stable constituent phases.[37] The energy of formation for each $Li_{(4-3x)}Y_xCl_4$ compound, the so-called energy above the hull, was defined with respect to the total energies of the stable constituent phases as

$$E_f = E_{Li_{4-3x}Y_xCl_4} - (4-3x)E_{LiCl} - xE_{YCl_3} \quad (1)$$

It is worth pointing out that many of the experimentally reported SSE compounds are in fact metastable at 0 K,[53] including the well-known systems such as LGPS, Li_3OCl and Li_6PS_5Cl.[14,54,55] It is postulated that phases metastable at 0 K could be readily made in practice, so long as the energy above the hull is less than 0.03 eV per atom to accommodate the thermal fluctuation energy corresponding to room temperature.[53]

The Alloy-Theoretic Automated Toolkit (ATAT) is used to identify phases of the lowest total energy at each composition, through global energy minimization over designated composition ranges, with energetic terms being assessed using the linked VASP code. The resultant total energies were used to predict electrochemical potentials, with details of basic principles being extensively covered in a recent paper.[56] The average electrochemical potential $\bar{V}_{A\rightarrow B}$, for the transition between state A ($Li_x\Pi$) and state B ($Li_{x+\Delta x}\Pi$), with reference to the electrochemical potential of Li/Li^+ is:

$$\bar{V}_{A\rightarrow B} = -1/z\{[E_{total}(Li_{x+\Delta x}\Pi) - E_{total}(Li_x\Pi)]/\Delta x - E_{total}(Li)\} \quad (2)$$

where x is the number of Li atoms in the formula unit of $Li_x\Pi$, charge value $z = 1$ for Li^+, Δx is the change in the number of Li atoms, and Π refers to the collection of other constituents.

Ab initio molecular dynamics (AIMD) was carried out to quantify ionic diffusivity.[6,35,57,58] Each AIMD task was performed on conventional cells containing around 54 atoms depending on the stoichiometric formula over 180 ps after a pre-equilibrium run for 10 ps, using a time step of 2 fs in the NVT ensembles. AIMD data were obtained at elevated temperatures

from 600 K up to 900 K, in order to achieve steady state for ionic migration over affordable simulation time (as is shown in Fig. S1,† long range hopping of Li^+ is not observable below 600 K). The diffusion coefficient is related to the average mean square displacement (MSD) from molecular dynamics (MD) runs at each temperature T over a period of time (t), $\langle[\Delta r(t)]^2\rangle$, as

$$D = \langle[\Delta r(t)]^2\rangle/2dt \quad (3)$$

where d is the dimensionality factor ($d = 3$ in three dimensional diffused materials). Lower temperature data can then be derived by extrapolation from the Arrhenius equation $D = D_0 \cdot \exp(-E_a/k_BT)$, with D_0 (pre-exponential factor) and E_a (activation energy) which are constants for each AIMD system and can be obtained *via* plotting the logarithmic values of D against $1000/T$. The ionic conductivity is dictated by the diffusivity, *via* the Nernst–Einstein relationship. Correction of the MSD from artefactual errors due to the periodic boundary condition is necessary for a dependable AIMD evaluation of D,[59] using the "unwrapped" trajectories to help achieve a significant improvement in the sampling statistics from limited simulation data typical of tractable AIMD runs.[58]

Results and discussion

Structural relationship between Li3/1/6 and Li2/1/4 phases

Fig. 1(a) shows the structural configuration of Li_3YCl_6, with its ilmenite-like trigonal structure (space group $P\bar{3}21$ no. 150) being presented in a conventional hexagonal lattice. The lattice is made of octahedral YCl_6 and $LiCl_6$ units, through their layered arrangement along the c-axis with shared edges or facets of neighboring octahedra to achieve charge neutrality in the extended lattice. Vacancies (vac) on the metallic sites (Li or Y) are necessary to achieve overall charge neutrality, when the structure is arranged into a cubic lattice. It is interesting to note that the stable LiCl phase is made of only the octahedral $LiCl_6$ units arranged on a cubic lattice.

In the typical cubic spinel phase of Li_2MCl_4 (M: Cr) in Fig. 1(b), the mole ratio of Li : M : Cl is 2 : 1 : 4 with a diamond symmetry of $Fd\bar{3}m(227)$. The nominal valency of M in such a Li2/1/4 phase is +2, so as to maintain the charge neutrality. It is worth pointing out that transition metal ions can have different valency charges depending on the host structures.

Using ATAT simulation for global energy minimization, we find that the symmetry of the initially assumed cubic lattice (with a_c, b_c, and c_c as axes) for Li_2CrCl_4 is distorted into an orthorhombic one (with axes of a_o, b_o, and c_o), owing to adjustment/relaxation of the coordinates of constituent ionic species. The lattice framework is shown in Fig. 1(c), and such a spinel-like structure is of body-centered symmetry *Imma* (space group number 74). This is consistent with data from the Materials Project webpage (weblink: https://www.materialsproject.org), in that typical Li2/1/4 compounds such as Li_2CoCl_4 (mp-1222796), Li_2MgCl_4 (mp-38684), Li_2VCl_4 (mp-36330), Li_2MnCl_4 (mp-34148), Li_2FeCl_4 (mp-1222745), Li_2CdCl_4 (mp-38008), and Li_2CrCl_4 do have the same *Imma* lattice symmetry. The orientation relationships between the cubic and orthorhombic phases are indicated in Fig. 1(c), and the resultant conventional and primitive cells of the orthorhombic Li_2YCl_4 are also shown in Fig. 1(d) and (e), respectively. It is worth noting that DFT simulation results in slight orthorhombic distortion, while experimentally reported structures were cubic. This is a recognized issue attributable to the limited system sizes exploited in tractable DFT simulation, which could not reflect random mixing on the sites for both Li and M cations.

The question is whether it is energetically possible for the formation of such a spinel type of structure when the M sites are replaced by Y cations. If so, can one achieve significant improvement in terms of ionic conductivity and electrochemical performance at the same time? Extensive efforts have thus been made toward identifying potential SSEs around Li3/1/6 and Li2/1/4, in line with the road-chart shown in Fig. 2.

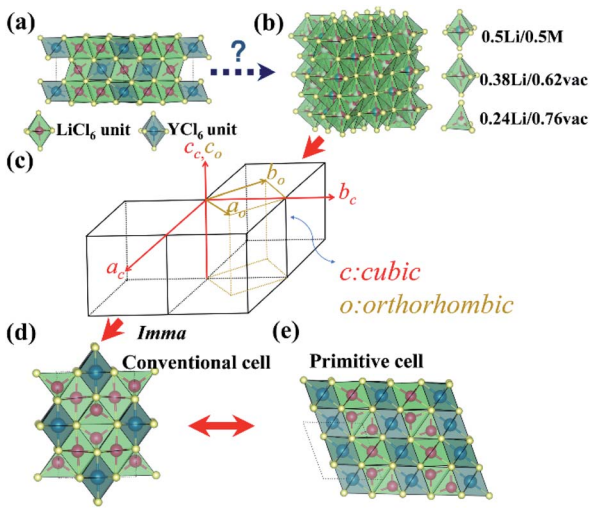

Fig. 1 Schematic mechanism and crystallographic relationship: the most stable structural changes from a typical hcp phase of (a) Li_3YCl_6 to a cubic spinel configuration of (b) Li_2MCl_4. (c) a_c, b_c, and c_c are the axes for the cubic spinel phase, while a_o, b_o, and c_o are the axes for the orthorhombic phase. (d) The conventional cell of Li_2MCl_4 reduced from the cubic spinel phase, while (e) is the primitive cell of Li_2MCl_4.

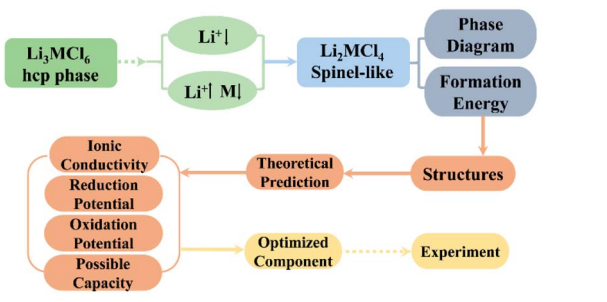

Fig. 2 The overall flow chart explores the route for the transformation of hcp into the spinel phase based on the off-stoichiometric compositions as well as theoretically predicts the critical aspects of the performances of SSE for the selected compounds.

Tuning of lattice chemistry to identify spinel-like phases

Fig. 3(a) shows the phase diagram of Li_3YCl_6 with their corresponding stable constituent phases of LiCl (mp-22905), Y_2Cl_3 (mp-27678), YCl_3 (mp-27455), and Cl_2 gas. The formation energy of Li_3YCl_6 is 0.0171 eV/atom referring to LiCl and YCl_3 ($3LiCl + YCl_3 \rightarrow Li_3YCl_6$), being lower than the criterion of 0.03 eV per atom. However, the formation energy for the spinel-like Li_2YCl_4 phase ($2LiCl + (1/3)YCl_3 + (1/3)Y_2Cl_3 \rightarrow Li_2YCl_4$) is found to be over two times that of the 0.03 eV per atom threshold, being 0.0717 eV per atom, indicating considerable difficulty in experimental realization.

Through tuning the chemical composition along the direction indicated along the red arrow in Fig. 3(a), a series of low-energy compounds $Li_{(2-x)}YCl_4$ ($0 \leq x \leq 1$) are identified with the pseudo-convex hull, with reference to the two metastable compounds, being shown in Fig. 3(b). These phases are not considered to be adequately stable with reference to the stable constituent phases listed in Table S1.† All phases have formation energies over 0.03 eV per atom above the stable hull with the lowest energy phase having a formation energy of 0.04 eV per atom with reference to the stable constituents, Fig. 3(c), even though considerable stabilization is achieved from mixing the two terminal metastable phases.

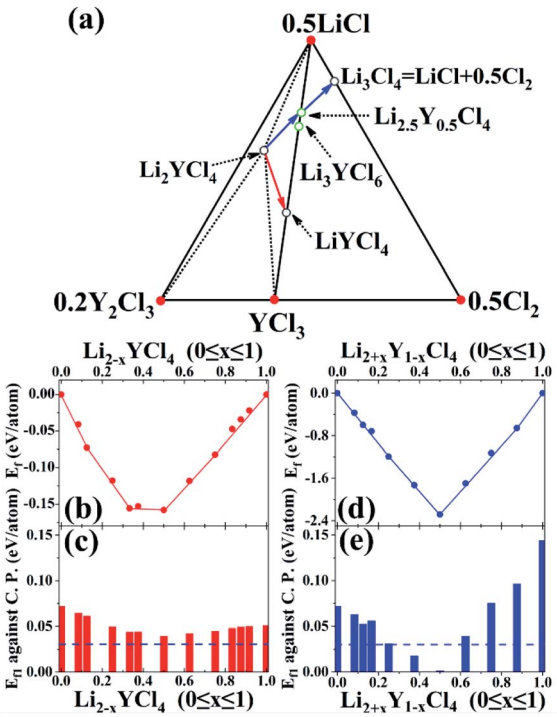

Fig. 3 (a) Phase diagram of the candidates of $Li_{(4-3x)}Y_xCl_4$ being in equilibrium with associated constituent phases at 0 K, in which the blue and red arrows represent the searching direction. (b) Convex hull from Li^+ depletion in $Li_{2-x}YCl_4$ ($0 \leq x \leq 1$), and (c) the corresponding formation energies of the stable states on/close to the edge of the convex hull. (d) Convex hull from Li^+ partially occupying the Y^{3+} site in $Li_{2+x}Y_{1-x}Cl_4$ ($0 \leq x \leq 1$), and (e) the corresponding formation energies of the stable states on/close to the edge of the convex hull. The dashed lines in (c) and (e) represent the criteria of 0.03 eV per atom.

Alternately, by searching along the path indicated by the blue arrow in Fig. 3(a), a series of off-stoichiometric compounds $Li_{2+x}Y_{1-x}Cl_4$ ($0 \leq x \leq 1$) are identified as the lowest energy structures (listed in Table S2†). A pseudo-convex hull, exhibited in Fig. 3(d), is constructed by the lowest energy phases with Li^+ partially occupying Y^{3+} sites. Similarly, with reference to the stable constituent phases (listed in Table S2†), the equilibrium formation energies of the compounds are derived as shown in Fig. 3(e). The formation energies of the off-stoichiometric compounds $Li_{2.25}Y_{0.75}Cl_4$, $Li_{2.375}Y_{0.625}Cl_4$, and $Li_{2.5}Y_{0.5}Cl_4$ are found to be 0.031, 0.0176, and 0.00135 eV per atom above the stable hull, respectively. It is worth pointing out that the formation energy of the last compound can be considered to be on the stable energy hull, as the accuracy of the DFT calculation is largely limited to the order of meV per atom. Apparently, partial occupancy of the Y^{3+} sites by Li^+ ions leads to a significant stabilization effect, making the identified spinel-like structures of $Li_{2+x}Y_{1-x}Cl_4$ almost completely stable.

It is intriguing to note that phases get more and more stable with reference to stable constituent phases, with their compositions, $Li_{2.25}Y_{0.75}Cl_4$, $Li_{2.375}Y_{0.625}Cl_4$, and $Li_{2.5}Y_{0.5}Cl_4$, approaching the straight line between two stable constituent phases LiCl and YCl_3, Fig. 4(a). The most stable of these three phases, $Li_{2.5}Y_{0.5}Cl_4$, joins the hexagonal Li_3YCl_6 on this straight line with end terminal stable binary phases of LiCl and YCl_3. Further de-lithiation will destabilize the phase and lead to decomposition, as shown in Fig. S2 and Table S3,† which is not desirable due to the tendency to release chlorine gas beyond the LiCl–YCl_3 border line. This confirms again that mixing between stable constituents could be a more likely scheme in search of stable multi-component compounds, which is in accordance with the well-recognized thermodynamic principle owing to the reduced level of energy of mixing.[60] Interestingly, de-lithiation of $Li_{2.25}Y_{0.75}Cl_4$ and $Li_{2.375}Y_{0.625}Cl_4$ towards the stable LiCl–YCl_3 constituent line leads to spinel-like $Li_{1.75}Y_{0.75}Cl_4$ (Fig. 4(b)) and $Li_{2.125}Y_{0.625}Cl_4$ (Fig. 4(d)) phases, with their formation energies being close to the stable energy hull. Corresponding data are listed in Tables S4 and S5,† and one can see that further

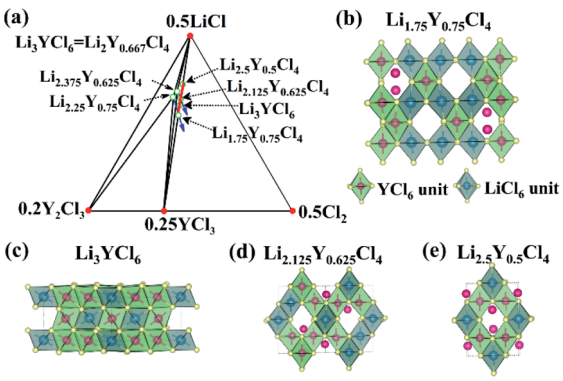

Fig. 4 (a) Phase diagram of the selected compounds $Li_{1.75}Y_{0.75}Cl_4$, Li_3YCl_6, $Li_{2.125}Y_{0.625}Cl_4$, and $Li_{2.5}Y_{0.5}Cl_4$. Associated configurations are displayed in (b), (c), (d) and (e), respectively. The blue arrows in (a) indicate the further de-lithiation states of $Li_{1.75}Y_{0.75}Cl_4$ and $Li_{2.125}Y_{0.625}Cl_4$ from $Li_{2.25}Y_{0.75}Cl_4$ and $Li_{2.375}Y_{0.625}Cl_4$.

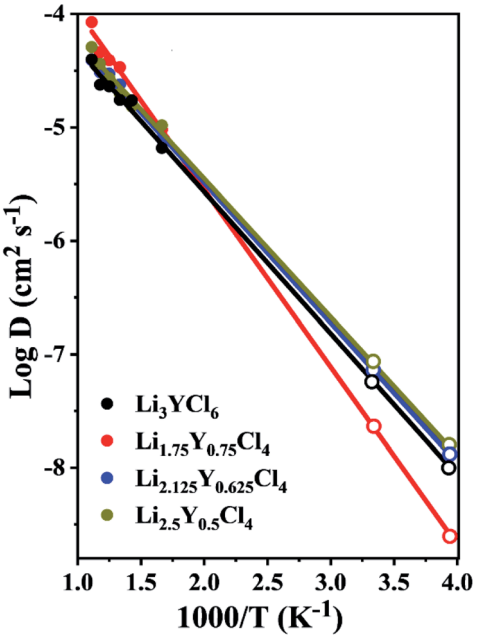

Fig. 5 Diffusion coefficients for Li^+ ions in various alloys, predicted by AIMD simulation.

de-lithiation beyond the stable LiCl–YCl_3 constituent border line leads to increased energetic drive for phase decomposition. As is shown in Table S6,† this border line also applies to the hexagonal Li_3YCl_6 phase. As is evidenced by the ATAT result in Fig. S3(a),† there is a tendency for structural collapse of Li_3YCl_6 when it is depleted of Li^+ ions, with the formation of the Li-lean $Li_{5/3}YCl_6$ being as high as 0.0648 eV per atom. This is indicative of potential decomposition of $Li_{5/3}YCl_6$ into the constituent phases.

In summary, three low-energy compounds, $Li_{1.75}Y_{0.75}Cl_4$ (Fig. 4(b)), $Li_{2.125}Y_{0.625}Cl_4$ (Fig. 4(d)), and $Li_{2.5}Y_{0.5}Cl_4$ (Fig. 4(e)), have been identified with formation energies very close to the corresponding energies of the stable constituents of LiCl and YCl_3. Energetically they are more stable than the hexagonal Li_3YCl_6 (0.0171 eV per atom, Fig. 4(c)), which were successfully synthesized.[22] All of the three newly identified phases have similar spinel-like structures, with structural parameters and space group information listed in Table S7.† Together with the hexagonal Li_3YCl_6 phase, they all result from mixing of the two stable constituents LiCl and YCl_3, by compensation of Y and Li as cations in the lattice. The overall charge neutrality is maintained due to inheritance of charge balance in the constituent species. The 0.5LiCl–YCl_3 line defines a border for preferable stability, beyond which, the tendency for phase decomposition and release of gaseous Cl_2 will increase, Fig. 4(a). As an example, such a case is demonstrated by de-lithiation of the Li_3YCl_6 phase, when the low-energy structure of the lost symmetry with broken chemical bonds would become more stable than the cubic spinel phase, once the composition is shifted beyond the 0.5LiCl–YCl_3 border, as shown in Fig. S3.†

Li^+ transportation

The Li^+ diffusion data are presented in Fig. 5, by plotting the logarithmic value of *D versus* the reverse of temperature 1000/*T*. The linear correlation is typical of an Arrhenius relationship, thus resulting in activation energies and extrapolated lower temperature data. The derived ionic conductivity data are summarized in Table 1. And the ionic conductivities of Li_3YCl_6 and various alloys at 300 K to 900 K from AIMD simulations are summarized in Table S8.† The Li^+ ion conductivity for the hexagonal phase of Li_3YCl_6 is predicted to be 4.22 mS cm^{-1} at room temperature (300 K) with an activation barrier of 0.256 eV. The theoretical conductivity is better and the activation energy is lower than the experimentally reported value (0.51 mS cm^{-1}, 0.4 eV), possibly due to widely reported boundary issues in practical polycrystalline materials. For tractable AIMD simulation, microscopical defects such as grain or particle boundaries cannot yet be considered. AIMD simulation of the spinel-like $Li_{1.75}Y_{0.75}Cl_4$ results in an ionic conductivity of 1.59 mS cm^{-1} at 300 K and a higher activation barrier of 0.313 eV. For the spinel-like $Li_{2.125}Y_{0.625}Cl_4$ and $Li_{2.5}Y_{0.5}Cl_4$ with higher Li^+ concentrations, the activation energy is lowered to about 0.247 eV, and the room-temperature Li^+ conductivities are boosted up to 6.11 and 8.42 mS cm^{-1} respectively. The low activation energy of about 0.256 eV and significant room-temperature conductivities enable ionic conductivity above 1 mS cm^{-1} even at 253 K (−20 °C), which is highly desirable for feasible solid-state battery technologies.

The Li^+ trajectories in the Li_3YCl_6, $Li_{1.75}Y_{0.75}Cl_4$, $Li_{2.125}Y_{0.625}Cl_4$, and $Li_{2.5}Y_{0.5}Cl_4$ phases determined by AIMD simulations are shown in Fig. 6 in (a), (b), (c) and (d), respectively. It is seen from Fig. 6(a) that there exist continuous Li^+ diffusion channels in Li_3YCl_6. The Li^+ ions can hop between neighboring octahedral units or along the edges of face-sharing octahedral sites (Fig. 6(a′)) to form a major one-dimensional (1D) pathway for Li^+ transportation along the vertical *c*-axis. These 1D channels are connected through *ab*-planes forming a three-dimensional (3D) diffusion network for Li ions. In the spinel-like phase (Fig. 6 (b) to (d)), Li^+ diffusion pathways are in

Table 1 Summary of data for the activation barrier of E_a (eV), Arrhenius prefactor D_0 (cm^{-2} s^{-1}), ionic diffusion coefficient D (cm^{-2} s^{-1}), and conductivity σ (mS cm^{-1}) at 300 K/253 K in this work

Compounds	E_a (eV)	D_0 (cm^{-2} s^{-1})	D_{300} (cm^{-2} s^{-1})	ρ (mol cm^{-3})	σ_{300K} (mS cm^{-1})	σ_{253K} (mS cm^{-1})
Li_3YCl_6	0.256	9.11×10^{-4}	5.009×10^{-8}	0.02244	4.22	0.809
$Li_{1.75}Y_{0.75}Cl_4$	0.313	3.85×10^{-3}	2.313×10^{-8}	0.01831	1.59	0.335
$Li_{2.125}Y_{0.625}Cl_4$	0.247	9.62×10^{-4}	7.317×10^{-8}	0.02221	6.11	1.243
$Li_{2.5}Y_{0.5}Cl_4$	0.244	9.72×10^{-4}	8.308×10^{-8}	0.02698	8.42	1.752

the form of an equivalent 3D network, where a Li^+ hops to another octahedral unit through a tetrahedral site in between, Fig. 6(d′). Trajectories in the better Li^+ ion conductors $Li_{2.125}Y_{0.625}Cl_4$, and $Li_{2.5}Y_{0.5}Cl_4$ (Fig. 6(c) and (d)) are more continuous than that of $Li_{1.75}Y_{0.75}Cl_4$ (Fig. 6(b)). This shows that the higher Li^+ concentration in the spinel phase is helpful in weakening electrostatic interaction between anions and cations, making Li^+ hopping easier. The spinel-like structural frameworks exhibit high stability according to AIMD at elevated temperatures, and their edge-sharing octahedra are expected to be advantageous in maintaining structural integrity over change of lithium content on charging–discharging.

Reduction and oxidation potential

The thermodynamic stability between the identified SSEs and anode can be assessed on the basis of interfacial reactions. While Li can be in direct equilibrium with LiCl, the other constituent halides YCl_3 and Y_2Cl_3 tend to react with Li to release Y, due to the lack of stable metallic compounds between Y and Li metals, as is shown in Fig. S4.† Taking Li_3YCl_6 and $Li_{2.5}Y_{0.5}Cl_4$ as examples,

$$Li_3YCl_6 + 3Li \rightarrow 6LiCl + Y \quad (4)$$

$$Li_3YCl_6 + (3/2)Li \rightarrow 4.5LiCl + 0.5Y_2Cl_3 \quad (5)$$

$$Li_{2.5}Y_{0.5}Cl_4 + 1.5Li \rightarrow 4LiCl + 0.5Y \quad (6)$$

$$Li_{2.5}Y_{0.5}Cl_4 + 0.75Li \rightarrow 3.25LiCl + 0.25Y_2Cl_3 \quad (7)$$

The reaction energy (E_R) can be readily assessed from the energies of products and reactants, $E_R = (E_{products} - E_{reactants})/n$, where n is the number of atoms. On the basis of the aforementioned ATAT results, there is a series of potential compounds $Li_{2.125+x}Y_{0.625}Cl_4$ ($0 \le x \le 0.25$) or $Li_{1.75+x}Y_{0.75}Cl_4$ ($0 \le x \le 0.5$) on the Li-rich side, so that the interfacial stabilities of Li-rich compositions against Li metal can be identified as:

$$Li_{2.375}Y_{0.625}Cl_4 + 1.625Li \rightarrow 4LiCl + (0.625)Y \quad (8)$$

$$Li_{2.375}Y_{0.625}Cl_4 + 0.6875Li \rightarrow 3.0625LiCl + (0.3125)Y_2Cl_3 \quad (9)$$

$$Li_{2.25}Y_{0.75}Cl_4 + 1.75Li \rightarrow 4LiCl + 0.75Y \quad (10)$$

$$Li_{2.25}Y_{0.75}Cl_4 + 0.625Li \rightarrow 2.875LiCl + 0.375Y_2Cl_3 \quad (11)$$

The energy changes for these reactions are all negative, as listed in Table S9.† The reduction energies of the identified SSEs are about 0.579 V (Table 2), according to eqn (1), and this indicates the potential need to utilize buffer layers to isolate SSEs from the Li anode.[61,62]

Based on total energies from ATAT simulations, the electrochemical potential *vs.* Li/Li^+ for each structural configuration can be obtained. A high oxidation potential is essential to prevent cathode–electrolyte interfacial reactions during de-lithiation.[6] Rather stable SSEs exist on the $LiCl–YCl_3$ line, and this is of potential importance since any limited de-lithiation of the best electrolyte $Li_{2.5}Y_{0.5}Cl_4$ tends to result in the formation of other stable phases of lower lithium contents. The oxidation potentials for this series of identified phases can be readily derived from the total energies on phases along the $LiCl–YCl_3$ line. In particular, they rank in the following order: Li_3YCl_6 (4 V), $Li_{2.5}Y_{0.5}Cl_4$ (4.05 V), $Li_{2.125}Y_{0.625}Cl_4$ (4.4 V), $Li_{1.75}Y_{0.75}Cl_4$ (4.56 V). It is worth pointing out that the three new spinel-like phases have nearly the same lattice parameters (Table S7†), suggesting little volumetric change owing to transitions between them. Their combined usage in the batteries, with the Li-rich phase as the electrolyte and the Li-lean one as coating for the cathode material, would be able to provide exceptionally high voltage tolerance, from 4.05 V to 4.56 V, which was shown only possible in oxide based solid electrolytes that however have very poor ionic conductivity. Such high ionic conductivity, low activation energy and oxidation potential higher than 4.05 V make this class of new solid-state electrolytes highly appealing to high energy density batteries, when use of high voltage cathodes is greatly advantageous.

Bandgap

SSEs should be insulating to electrons to avoid internal discharge. Fig. 7 presents the density of states (DOS) for the

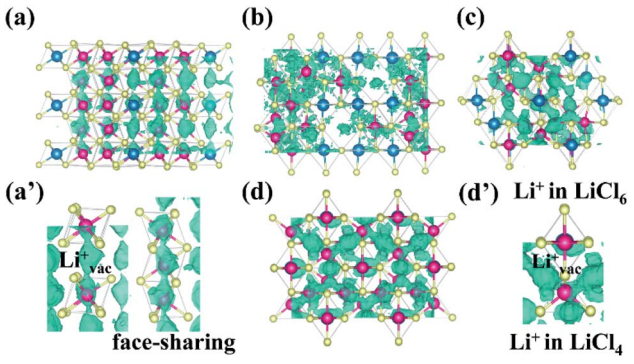

Fig. 6 The diffusion trajectories of Li^+ ions in (a) and (a′) hexagonal Li_3YCl_6, and in spinel-like (b) $Li_{1.75}Y_{0.75}Cl_4$, (c) $Li_{2.125}Y_{0.625}Cl_4$, and (d) and (d′) $Li_{2.5}Y_{0.5}Cl_4$, over a simulation time of 180 ps at 900 K.

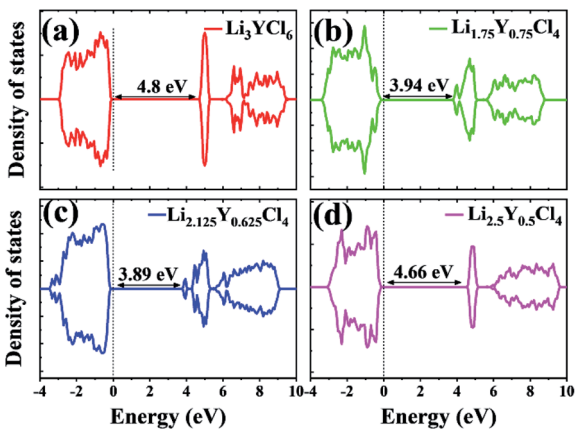

Fig. 7 Density of states (DOS) for the ionic conductors of interest in this work for (a) Li_3YCl_6, (b) $Li_{1.75}Y_{0.75}Cl_4$, (c) $Li_{2.125}Y_{0.625}Cl_4$, and (d) $Li_{2.5}Y_{0.5}Cl_4$.

Table 2 The electrochemical window of SSEs identified based on the associated equilibrium phases during lithiation and de-lithiation processes

States	Equilibrium phases	Voltage (V)
Li_3YCl_6 + 3Li	6LiCl + Y	0–0.509
Li_3YCl_6 + (3/2)Li	4.5LiCl + 0.5Y_2Cl_3	0.509–0.579
Li_3YCl_6	3LiCl + YCl_3	0.579–3.677
$Li_{5/3}YCl_6$	(5/3)LiCl + YCl_3 + (2/3) Cl_2	3.677–
$Li_{2.5}Y_{0.5}Cl_4$ + 1.5Li	4LiCl + 0.5Y	0–0.509
$Li_{2.5}Y_{0.5}Cl_4$ + 0.75Li	3.25LiCl + 0.25Y_2Cl_3	0.509–0.579
$Li_{2.5}Y_{0.5}Cl_4$	2.5LiCl + (0.5)YCl_3	0.579–3.677
$Li_{1.625}Y_{0.5}Cl_4$	1.625LiCl + (0.5)YCl_3 + (0.4375)Cl_2	3.677–
$Li_{2.375}Y_{0.625}Cl_4$ + 1.625Li	4LiCl + (0.625)Y	0–0.509
$Li_{2.375}Y_{0.625}Cl_4$ + 0.6875Li	3.0625LiCl + (0.3125) Y_2Cl_3	0.509–0.579
$Li_{2.375}Y_{0.625}Cl_4$	2.375LiCl + (11/24)YCl_3 + (1/12)Y_2Cl_3	0.579–0.579
$Li_{2.25}Y_{0.625}Cl_4$	2.25LiCl + (13/24)YCl_3 + (1/24)Y_2Cl_3	0.579–0.579
$Li_{2.125}Y_{0.625}Cl_4$	2.125LiCl + (0.625)YCl_3	0.579–3.677
$Li_2Y_{0.625}Cl_4$	2LiCl + (0.625)YCl_3 + (0.0625)Cl_2	3.677
$Li_{1.875}Y_{0.625}Cl_4$	1.875LiCl + (0.625)YCl_3 + (0.125)Cl_2	3.677–
$Li_{2.25}Y_{0.75}Cl_4$ + 1.75Li	4LiCl + 0.75Y	0–0.509
$Li_{2.25}Y_{0.75}Cl_4$ + 0.625Li	2.875LiCl + 0.375Y_2Cl_3	0.509–0.579
$Li_{2.25}Y_{0.75}Cl_4$	2.25LiCl + (5/12)YCl_3 + (1/6)Y_2Cl_3	0.579–0.579
$Li_2Y_{0.75}Cl_4$	2LiCl + (7/12)YCl_3 + (1/12)Y_2Cl_3	0.579–0.579
$Li_{31/16}Y_{0.75}Cl_4$	31/16LiCl + (5/8)YCl_3 + (1/16)Y_2Cl_3	0.579–0.579
$Li_{15/8}Y_{0.75}Cl_4$	15/8LiCl + (2/3)YCl_3 + (1/24)Y_2Cl_3	0.579–0.579
$Li_{1.75}Y_{0.75}Cl_4$	1.75LiCl + (3/4)YCl_3	0.579–3.677
$Li_{13/8}Y_{0.75}Cl_4$	13/8LiCl + (3/4)YCl_3 + (1/16)Cl_2	3.677–3.677
$Li_{1.5}Y_{0.75}Cl_4$	1.5LiCl + (3/4)YCl_3 + (1/8)Cl_2	3.677–

ionic conductors of interest in this work, using the HSE06 functional to account for the non-local effect. The band gaps of Li_3YCl_6, $Li_{1.75}Y_{0.75}Cl_4$, $Li_{2.125}Y_{0.625}Cl_4$, and $Li_{2.5}Y_{0.5}Cl_4$ are 4.8 eV, 3.94 eV, 3.89 eV, and 4.66 eV, respectively. They are obviously larger than those of well-known SSEs such as LGPS (2.68 eV) and Li_6PS_5Cl (3.1 eV),[14,54] which is highly advantageous in preventing electrical discharge in solid-state battery cells.

Conclusions

Through tuning of lattice chemistry in the hexagonal Li_3YCl_6 phase, we have identified three fairly stable spinel-like compounds with almost the same lattice parameters, $Li_{1.75}Y_{0.75}Cl_4$, $Li_{2.125}Y_{0.625}Cl_4$ and $Li_{2.5}Y_{0.5}Cl_4$, as potential solid-state electrolytes. $Li_{2.125}Y_{0.625}Cl_4$ and $Li_{2.5}Y_{0.5}Cl_4$ with higher Li contents are superb ionic conductors with 6.11 mS cm^{-1} and 8.42 mS cm^{-1} at 300 K, respectively, several times higher than that of the pristine Li_3YCl_6. The activation energies of $Li_{2.125}Y_{0.625}Cl_4$ and $Li_{2.5}Y_{0.5}Cl_4$ are lower than 0.247 eV, which is beneficial to ensure adequate ionic conductivities well below the room temperature.

The newly formulated compounds $Li_{1.75}Y_{0.75}Cl_4$, $Li_{2.125}Y_{0.625}Cl_4$ and $Li_{2.5}Y_{0.5}Cl_4$ have outstanding oxidation potentials above 4.05 V, making them electrochemically compatible with high-voltage cathodes desirable for high-energy-density batteries. Utilization of the spinel-like structures as both electrolyte and coating for active cathode materials is expected to offer both high resilience to voltage and good mechanical integrity, which is highly attractive for solid-state lithium ion batteries wherein mechanical integrity is very important over intercalation/de-intercalation of lithium ions.

Conflicts of interest

There are no conflicts to declare.

Acknowledgements

The work has been funded in part by the Zhengzhou Materials Genome Institute, the overseas talents program of China, and the National Natural Science Foundation of China (No. 51001091, 111174256, 91233101, 51602094, 11274100).

Notes and references

1 M. Tatsumisago, M. Nagao and A. Hayashi, *J. Asian Ceram. Soc.*, 2018, **1**, 17–25.
2 K. Takada, *Acta Mater.*, 2013, **61**, 759–770.
3 N. Kamaya, K. Homma, Y. Yamakawa, M. Hirayama, R. Kanno, M. Yonemura, T. Kamiyama, Y. Kato, S. Hama, K. Kawamoto and A. Mitsui, *Nat. Mater.*, 2011, **10**, 682–686.
4 R. Murugan, V. Thangadurai and W. Weppner, *Angew. Chem., Int. Ed.*, 2007, **46**, 7778–7781.
5 Z. Wang and G. Shao, *J. Mater. Chem. A*, 2017, **5**, 21846–21857.
6 M. Xuan, W. Xiao, H. Xu, Y. Shen, Z. Li, S. Zhang, Z. Wang and G. Shao, *J. Mater. Chem. A*, 2018, **6**, 19231–19240.
7 X. Han, Y. Gong, K. Fu, X. He, G. T. Hitz, J. Dai, A. Pearse, B. Liu, H. Wang, G. Rubloff, Y. Mo, V. Thangadurai, E. D. Wachsman and L. Hu, *Nat. Mater.*, 2016, **16**, 572–579.
8 Y. Deng, C. Eames, J. N. Chotard, F. Lalere, V. Seznec, S. Emge, O. Pecher, C. P. Grey, C. Masquelier and M. S. Islam, *J. Am. Chem. Soc.*, 2015, **137**, 9136–9145.
9 G. Liu, D. Xie, X. Wang, X. Yao, S. Chen, R. Xiao, H. Li and X. Xu, *Energy Storage Mater.*, 2019, **17**, 266–274.
10 Y. Li, J. Han, C. Wang, H. Xie and J. B. Goodenough, *J. Mater. Chem.*, 2012, **22**, 15357–15361.
11 C.-L. Tsai, V. Roddatis, C. V. Chandran, Q. Ma, S. Uhlenbruck, M. Bram, P. Heitjans and O. Guillon, *ACS Appl. Mater. Interfaces*, 2016, **8**, 10617–10626.
12 D. Wang, Q. Sun, J. Luo, J. Liang, Y. Sun, R. Li, K. Adair, L. Zhang, R. Yang, S. Lu, H. Huang and X. Sun, *ACS Appl. Mater. Interfaces*, 2019, **11**, 4954–4961.

13 S. Yu, R. D. Schmidt, R. Garcia-Mendez, E. Herbert, N. J. Dudney, J. B. Wolfenstine, J. Sakamoto and D. J. Siegel, *Chem. Mater.*, 2016, **28**, 197–206.
14 H.-J. Deiseroth, S.-T. Kong, H. Eckert, J. Vannahme, C. Reiner, T. Zaiß and M. Schlosser, *Angew. Chem., Int. Ed.*, 2008, **47**, 755–758.
15 Y. J. Nam, D. Y. Oh, S. H. Jung and Y. S. Jung, *J. Power Sources*, 2018, **375**, 93–101.
16 A. Sakuda, A. Hayashi and M. Tatsumisago, *Sci. Rep.*, 2013, **3**, 2261.
17 X. Li, Z. Ren, M. Norouzi Banis, S. Deng, Y. Zhao, Q. Sun, C. Wang, X. Yang, W. Li, J. Liang, X. Li, Y. Sun, K. Adair, R. Li, Y. Hu, T.-K. Sham, H. Huang, L. Zhang, S. Lu, J. Luo and X. Sun, *ACS Energy Lett.*, 2019, **4**, 2480–2488.
18 Y. Zhu, X. He and Y. Mo, *J. Mater. Chem. A*, 2016, **4**, 3253–3266.
19 C. C. Liang, *J. Electrochem. Soc.*, 1971, **118**, 894–895.
20 C. C. Liang, J. Epstein and G. H. Boyle, *J. Electrochem. Soc.*, 1969, **116**, 1322–1323.
21 C. J. J. Van Loon and J. De Jong, *Acta Crystallogr., Sect. B: Struct. Crystallogr. Cryst. Chem.*, 1975, **31**, 2549–2550.
22 T. Asano, A. Sakai, S. Ouchi, M. Sakaida, A. Miyazaki and S. Hasegawa, *Adv. Mater.*, 2018, **30**, 1803075.
23 X. Li, J. Liang, N. Chen, J. Luo, K. R. Adair, C. Wang, M. N. Banis, T.-K. Sham, L. Zhang, S. Zhao, S. Lu, H. Huang, R. Li and X. Sun, *Angew. Chem., Int. Ed.*, 2019, **58**, 16427–16432.
24 R. D. Shannon, *Acta Crystallogr., Sect. A: Cryst. Phys., Diffr., Theor. Gen. Crystallogr.*, 1976, **32**, 751.
25 K. S. Pitzer, *J. Am. Chem. Soc.*, 1960, **82**, 4121.
26 W. D. Richards, L. J. Miara, Y. Wang, J. C. Kim and G. Ceder, *Chem. Mater.*, 2016, **28**, 266–273.
27 X. Li, J. Liang, J. Luo, M. Norouzi Banis, C. Wang, W. Li, S. Deng, C. Yu, F. Zhao, Y. Hu, T.-K. Sham, L. Zhang, S. Zhao, S. Lu, H. Huang, R. Li, K. R. Adair and X. Sun, *Energy Environ. Sci.*, 2019, **12**, 2665–2671.
28 X. Li, J. Liang, K. R. Adair, J. Li, W. Li, F. Zhao, Y. Hu, T.-K. Sham, L. Zhang, S. Zhao, S. Lu, H. Huang, R. Li, N. Chen and X. Sun, *Nano Lett.*, 2020, **20**, 4384–4392.
29 K. Yamada, K. Iwaki, T. Okuda and Y. Tomita, *Solid State Ionics*, 2002, 621–628.
30 Y. Tomita, A. Fuji-i, H. Ohki, K. Yamada and T. Okuda, *Chem. Lett.*, 1998, **27**, 223–224.
31 H. D. Lutz, P. Kuske and K. Wussow, *Chem. Inf.*, 1986, **17**(49), 10.
32 R. Kanno, Y. Takeda, A. Matsumoto, O. Yamamoto, R. Suyama and S. Kume, *J. Solid State Chem.*, 1988, **75**, 41–51.
33 J. Liang, X. Li, S. Wang, K. R. Adair, W. Li, Y. Zhao, C. Wang, Y. Hu, L. Zhang, S. Zhao, S. Lu, H. Huang, R. Li, Y. Mo and X. Sun, *J. Am. Chem. Soc.*, 2020, **142**, 7012–7022.
34 L. Zhou, C. Y. Kwok, A. Shyamsunder, Q. Zhang, X. Wu and L. F. Nazar, *Energy Environ. Sci.*, 2020, **13**, 2056–2063.
35 Z. Wang, H. Xu, M. Xuan and G. Shao, *J. Mater. Chem. A*, 2018, **6**, 73–83.
36 Y. Yu, Z. Wang and G. Shao, *J. Mater. Chem. A*, 2019, **7**, 10483–10493.
37 H. Xu, Y. Yu, Z. Wang and G. Shao, *Energy Environ. Mater.*, 2019, **2**, 234–250.
38 G. Kresse and J. Hafner, *Phys. Rev. B: Condens. Matter Mater. Phys.*, 1993, **47**, 558–561.
39 G. Kresse and J. Hafner, *Phys. Rev. B: Condens. Matter Mater. Phys.*, 1994, **49**, 14251–14269.
40 G. Kresse and J. Hafner, *Phys. Rev. B: Condens. Matter Mater. Phys.*, 1993, **48**, 13115–13118.
41 P. E. Blöchl, *Phys. Rev. B: Condens. Matter Mater. Phys.*, 1994, **50**, 17953–17979.
42 G. Kresse and D. Joubert, *Phys. Rev. B: Condens. Matter Mater. Phys.*, 1999, **59**, 1758–1775.
43 Y. Yu, Z. Wang and G. Shao, *J. Mater. Chem. A*, 2019, **7**, 21985–21996.
44 J. P. Perdew, K. Burke and M. Ernzerhof, *Phys. Rev. Lett.*, 1996, **77**, 3865–3868.
45 X. Zhang, Z. Wang and G. Shao, *J. Mater. Chem. A*, 2020, **8**, 11177–11187.
46 Y. Yu, Z. Wang and G. Shao, *J. Mater. Chem. A*, 2018, **6**, 19843–19852.
47 G. Shao, *J. Phys. Chem. C*, 2009, **113**, 6800–6808.
48 G. Shao, *J. Phys. Chem. C*, 2008, **112**, 18677–18685.
49 H. Xu, Y. Yu, Z. Wang and G. Shao, *J. Mater. Chem. A*, 2019, **7**, 5239–5247.
50 Z. Wang, M. Deng, X. Xia, Y. Gao and G. Shao, *Energy Environ. Mater.*, 2018, **1**, 174–178.
51 J. Heyd, G. E. Scuseria and M. Ernzerhof, *J. Chem. Phys.*, 2003, **118**, 8207–8215.
52 Q. Deng, Z. Wang, S. Wang and G. Shao, *J. Sol. Energy*, 2017, **158**, 654–662.
53 S. P. Ong, Y. Mo, W. D. Richards, L. Miara, H. S. Lee and G. Ceder, *Energy Environ. Sci.*, 2013, **6**, 148–156.
54 A. Kuhn, V. Duppel and B. V. Lotsch, *Energy Environ. Sci.*, 2013, **6**, 3548–3552.
55 M. H. Braga, J. A. Ferreira, V. Stockhausen, J. E. Oliveira and A. El-Azab, *J. Mater. Chem. A*, 2014, **2**, 5470–5480.
56 H. Xu, W. Xiao, Z. Wang, J. Hu and G. Shao, *J. Energy Chem.*, 2021, **59**, 229–241.
57 Z. Deng, Z. Zhu, I.-H. Chu and S. P. Ong, *Chem. Mater.*, 2017, **29**, 281–288.
58 M. V. Agnihotri, S. H. Chen, C. Beck and S. J. Singer, *J. Phys. Chem. B*, 2014, **118**, 8170–8178.
59 W. M. Choi, Y. H. Jo, S. S. Sohn, S. Lee and B. J. Lee, *npj Comput. Mater.*, 2018, **4**, 1–9.
60 N. Saunders and A. Miodownik, *Calphad (Calculation of Phase Diagrams) A Comprehensive Guide*, Pergamon, 1992.
61 X. Ji, S. Hou, P. Wang, X. He, N. Piao, J. Chen, X. Fan and C. Wang, *Adv. Mater.*, 2020, **32**, 2002741.
62 J. Sang, Y. Yu, Z. Wang and G. Shao, *Phys. Chem. Chem. Phys.*, 2020, **22**, 12918–12928.

